FFEMS Fatigue & Fracture of Engineering Materials & Structures

doi: 10.1111/ffe.12011

Static and fatigue characterization of the Ti5553 titanium alloy

M. B. BETTAIEB[1,*], A. LENAIN[2] and A. M. HABRAKEN[1,3]

[1]*Department ArGEnCo, Division MS²F, University of Liège, Chemin des Chevreuils 1, 4000 Liège, Belgium,* [2]*Techspace Aero, DT Matériaux & Procédés, Route de Liers 121, 4041 Milmort, Belgium,* [3]*FNRS Fond National de la Recherche Scientifique, Liége, Belgium*

Received in final form 27 July 2012

ABSTRACT This paper presents and discusses static (elastoviscoplastic and damage) and high-cycle fatigue characterization of two microstructures of the Ti5553 alloy. The difference between these two microstructures is related to their heat treatment and precisely to the temperature of the final aging. For each microstructure, several tests were carried out to identify their static and fatigue properties and the test results were correlated to the microstructure. A fractographic analysis of the rupture sections was performed in order to investigate the fracture mechanisms of the two microstructures. Finally, the fatigue properties of the two microstructures were compared with those found in results reported in the literature for two other classical titanium alloys used for aeronautical applications.

Keywords fractographic analysis; Goodman diagrams; high-cycle fatigue; static characterization; Ti5553 alloy.

NOMENCLATURE

HCF = High cycle fatigue
LCF = Low cycle fatigue
NR = the number of cycles to failure
P_1, P_2, P_3, P_4 = Norton Hoff parameters
S-N curve = the evolution of σ_a with NR
α = alpha metallurgical phase
β = beta metallurgical phase
$\bar{\varepsilon}$ = Von Mises equivalent strain
ε_{11} = True stress in the tensile direction
$\dot{\bar{\varepsilon}}$ = Von Mises equivalent strain rate
ε_f = Strain at fracture
σ_{11} = True strain in the tensile direction
$\bar{\sigma}$ = Von Mises equivalent stress
$\sigma_{p0.2}$ = yield stress computed at 0.2% of the plastic strain
σ_{min} = minimum stress imposed at each cycle
σ_{max} = maximum stress imposed at each cycle
σ_m = mean stress
σ_a = magnitude or alternated stress equal to $(\sigma_{max} - \sigma_{min})/2$

INTRODUCTION

Titanium alloys receive considerable interest due to their wide range of applications in the aerospace, automotive, chemical and medical industries.[1–6] These alloys are selected for their low density, their good corrosion behaviour and their excellent mechanical properties. The well-known Ti-6Al-4V has been the most commonly used titanium alloy for aerospace components (e.g. fan disks, spools) for almost 50 years. However, the need to increase the strength of Ti-6Al-4V components combined with the alloy's inherent limitation due to its hardenability has created interest in other titanium alloys. Over the past few years, several scientific and industrial teams have identified Ti5553 as a promising alloy.[7–10] Currently, little information is available regarding this relatively new alloy. Ti5553 is a high strength, near beta titanium alloy designed with excellent mechanical properties. It is a

Correspondence: M. B. Bettaieb. E-mail: Mohamed.BenBettaieb@ensicaen.fr
*Present address: Ensicaen, 6 Bd du Maréchal Juin, 14050 Caen, France

variation of the Russian alloy VT22[11] and is an alternative to the Ti-10–2-3 alloy. It provides a way of obtaining a microstructure of much greater strength than Ti-6Al-4V, leading to a lighter weight product.

Unfortunately, there is not a lot of information in the literature about the mechanical behaviour (static and fatigue properties) of the Ti5553 alloy, and present work gives some experimental results and explanations about its mechanical behaviour. The microstructure of the studied alloy is correlated with the mechanical properties. The current paper investigates whether the high strength and the good ductility of this alloy are associated with high fatigue properties. The first motivation behind the study is the fact that the majority of aerospace and automotive components are submitted to cyclic loading: high-cycle fatigue (HCF) and low cycle fatigue (LCF) loadings. The second motivation is related to the insufficiency of data in the literature regarding reliable structure design under fatigue loads.[10] Earlier studies have revealed a number of important factors underlying the fatigue behaviour of titanium alloys. It is reported in the literature[12–20] that the volume fraction and the morphology of the phases (α, β) in titanium alloys appear to be critical parameters for their mechanical properties in general and for their fatigue properties in particular. Indeed, the service life and reliability of these alloys depend on the microstructure obtained after hot working and final heat treatment and on the condition of the surface layer.[11,13,19,20]

In the present study, static (elastoviscoplasticity and damage) and high-cycle fatigue behaviour were investigated for two microstructures of the Ti5553 alloy, called hereafter Ti5553-1 and Ti5553-3. The first aging temperature of the heat treatment cycle was identical for the two microstructures. However the temperature of the second aging was different for each of the two microstructures: it was equal to 610 °C for the Ti5553-1 microstructure and 670 °C for the Ti5553-3 microstructure. This final aging was responsible for the nucleation of the secondary α phase. The temperature of this aging determined the volume fraction and the morphology of these α precipitates. These microstructures are correlated with the static and the fatigue properties.

A fractographic analysis was performed on fatigue specimens to understand the fracture mechanisms of the different microstructures. Finally, the fatigue behaviour of the Ti5553 alloy was also compared with the fatigue behaviour of two other classical titanium alloys (Ti40 and Ti-6Al-4V) used in the aeronautic industry.

The outline of the paper is as follows:

- Section 'Materials' describes the studied material (Ti5553 alloy), i.e. its chemical composition, heat treatment and microstructures;
- Section 'Elastoviscoplastic properties of the Ti5553 microstructures' presents the elastoviscoplastic properties of the two microstructures;
- Section 'Damage properties of the Ti5553 microstructures' details the damage properties of the Ti5553-1 and Ti5553-3 microstructures;
- Section 'Fatigue experiments and results' shows the fatigue experiments and results;
- Section 'Comparison of fatigue results of the two studied Ti5553 alloy microstructures with those of two other titanium alloys, Ti40 and Ti-6Al-4V' describes a comparison of the fatigue test results for both microstructures with that of other titanium alloys as described in results in the literature;
- Section 'Conclusions' presents some overall conclusions.

MATERIALS

General description of the studied microstructures

The Ti5553 (Ti-5Al-5V-5Mo-3Cr) alloy is a metastable β alloy. In fact, a large quantity of beta stabilizer elements such as Mo, V, Fe, Cr, etc. are present (see the chemical composition in Table 1). This alloy exhibits excellent hardenability and strength properties, making it attractive as a structural titanium alloy. Its transus temperature is about 860 °C. The Ti5553 alloy presents high sensitivity to the variation of the heat treatment and the thermomechanical treatment. This sensitivity has a significant impact on the microstructure as demonstrated in section 'Forging and heat treatment'.

As received material

The material used for the current study was a titanium alloy received from the Techspace Aero company (a member of the Safran group) in the form of forged pancakes (Fig. 1). The forging of these pancakes was performed at 815 °C on a 2500 ton forging press. The final thickness of these pancakes was equal to 47 mm.

Table 1 Chemical composition of the Ti5553 alloy (values are in wt%)

	Mo	Zr	Fe	V	Si	Al	C
Bottom	4.82	<0.005	0.3	4.93	<0.03	5.26	0.009
Top	4.87	<0.005	0.3	4.94	<0.03	5.33	0.007
	O	N	Cr	Y	H		
Bottom	0.14	0.005	3.04	<0.001	0.006		
Top	0.14	0.004	3.05	<0.001	0.004		

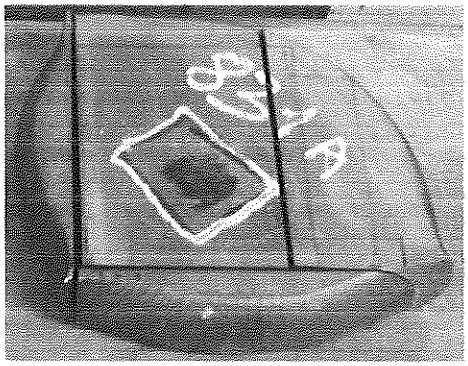

Fig. 1 Forged pancake.

Chemical composition of the billet

The measured chemical composition from the top and the bottom of the pancake is reported in Table 1.

The molybdenum equivalent (Mo equivalent) in terms of chemical composition is defined as follows:[21]

$$\begin{aligned} \text{wt\% Mo eq.} = {} & 1.0\ (\text{wt\% Mo}) + 0.66\ (\text{wt\% V}) \\ & + 0.33\ (\text{wt\% N}) + 3\ (\text{wt\% Fe}) \\ & + 3\ (\text{wt\% Cr}). \end{aligned} \quad (1)$$

Using the above table and formulae, the Mo equivalent of the present alloy was estimated (with the minimal composition) as 18.18.

Forging and heat treatment

The final heat treatment used to generate each Ti5553 microstructures studied is shown in Fig. 2.

A detailed description of the heat treatment cycle is given below:

- Ti5553-1: heat from room temperature up to 830 °C + hold at 830 °C for 2 h + air cooling + aging at 610 °C for 8 h + air cooling.

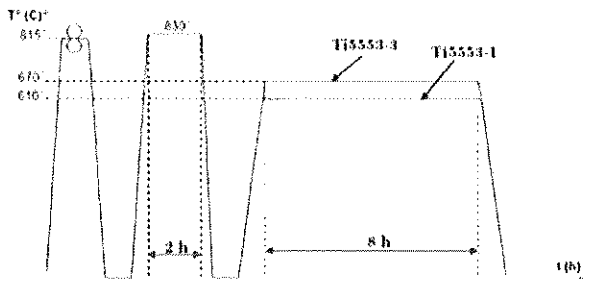

Fig. 2 Forging of pancakes and final heat treatment cycle applied to generate the two microstructures of Ti5553 alloy.

- Ti5553-3: heat from room temperature up to 830 °C + hold at 830 °C for 2 h + air cooling + aging at 670 °C for 8 h + air cooling.

Microstructures of the Ti5553 alloy

Figure 3 shows that the two generated microstructures are bi-modal, the primary α has a nodular morphology and the secondary α is lamellar. The first aging at 830 °C (Fig. 2) was responsible for the nucleation of the nodules of α. This aging was the same for both microstructures (Fig. 2), explaining why there is no difference between the morphology and the size of the nodular α phase of the two microstructures. The only difference between the two microstructures is related to the temperature of the final aging. This temperature was responsible for the formation of the secondary α phase, which contains particles shaped like needles or very small plates. For the microstructure Ti5553-1, as shown in Fig. 3 (a), this flat structure is slightly thinner (compared to the secondary α phase of the Ti5553-3 microstructure), due to a lower aging temperature (610 °C). In the Ti5553 alloy, the α phase is the main hardening mechanism. The size of the α particles has a significant effect on the static strength (section 'Elastoviscoplastic properties of the Ti5553 microstructures'), ductility (section 'Damage properties of the Ti5553 microstructures') and fatigue strength (section 'Fatigue experiments and results') of the studied microstructures.

ELASTOVISCOPLASTIC PROPERTIES OF THE TI5553 MICROSTRUCTURES

The mechanical behaviour of the two studied microstructures was previously determined in Refs [2, 3]. Both studies clearly demonstrate that the materials exhibit an elastoviscoplastic behaviour.

In order to investigate the elastoviscoplastic behaviour of the two microstructures at room temperature, four strain rates were investigated through different tests: 5×10^{-5} s^{-1}, 2×10^{-4} s^{-1}, 4×10^{-3} s^{-1} and 10^{-2} s^{-1}. To check experiment repeatability, three duplicate tests were performed for each strain rate and each microstructure.

Elastic behaviour

From several mechanical tests (uniaxial tensile tests at different strain rates and in different loading directions, plane strain tests, shear tests), it was previously demonstrated in Ref. [2] that the elastic behaviour of the two microstructures is isotropic and independent of the strain rate. Young's modulus was found in the present study to be equal to 112 GPa and 108 GPa for the Ti5553-1 and Ti5553-3 microstructures, respectively. These were

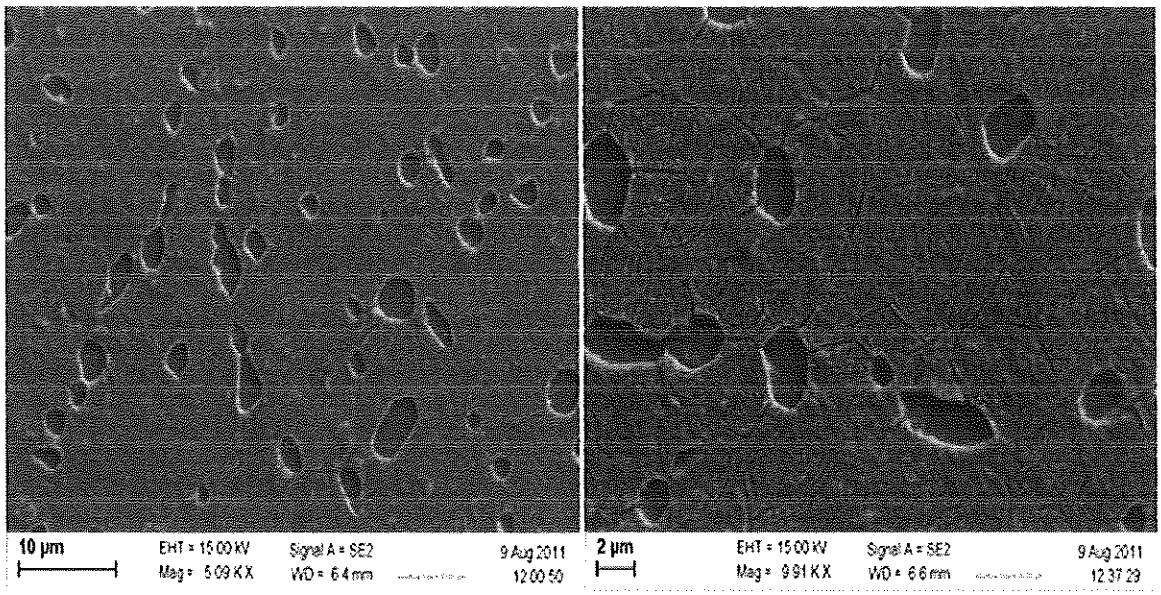

(a)

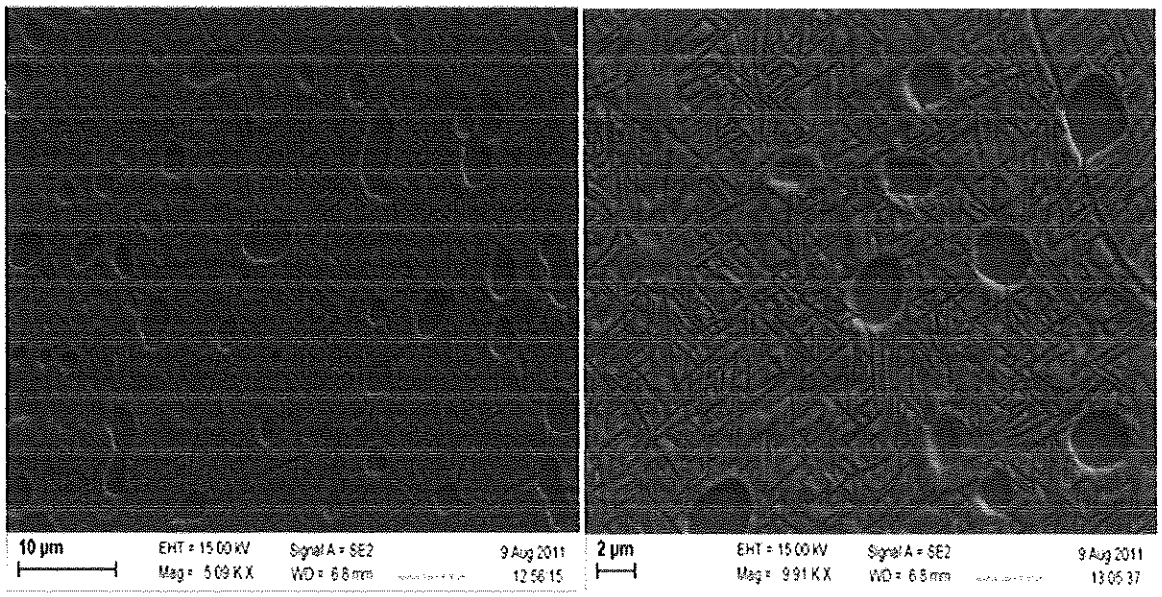

(b)

Fig. 3 Microstructures of the Ti5553 alloy. (a) Ti5553-1, (b) Ti5553-3.

average values calculated from 12 specimens (four strain rates and three specimens by strain rate) for each microstructure. Poisson's ratio was found to be equal to 0.35 for both microstructures (calculated from 2 tensile specimens for each microstructure). This ratio was measured by adding a radial extensometer to the axial extensometer used classically to measure the axial strain in the tensile direction.

Viscoplastic behaviour

Figure 4 (a) and (b) shows the effect of the strain rate on the viscoplatic behaviour of both microstructures. The values shown in the small box in Fig. 4 (a) and (b) (0.00005; 0.0002; 0.004; 0.01) define the strain rates expressed in s^{-1} used to perform the tensile tests. In order to accurately analyze the effect of the strain rate on the stress–strain curve, a magnification of the stress domain (1000 MPa,

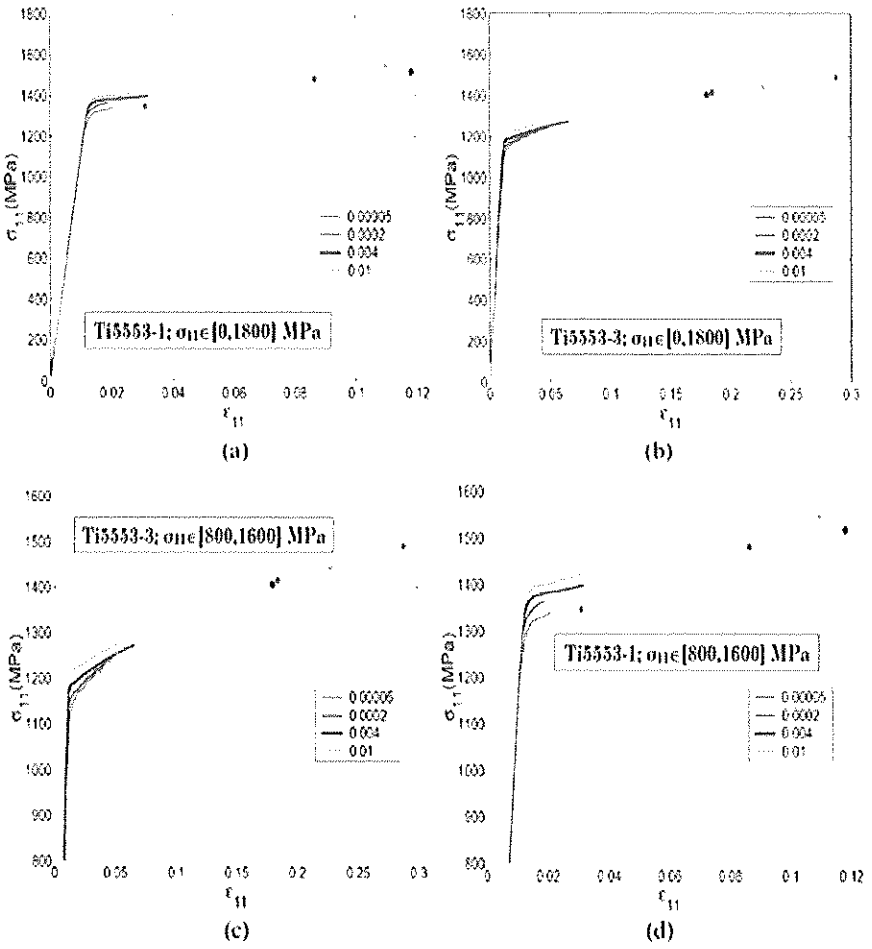

Fig. 4 Effect of the strain rate on the stress–strain curves.

1600 MPa) is shown in Fig. 4 (c) and (d). Only the average curve over the three duplicate specimens is presented. It is clear, for both microstructures, that strength increases with the strain rate. In Ref. [2], it was demonstrated (on the basis of several mechanical tests such as shear, compression and plane strain tensile tests) that the plasticity for both microstructures can be assumed to be isotropic and follows the Von Mises yield function. Figure 5 shows that the strength of Ti5553-1 is higher than the strength of Ti5553-3. The viscoplastic properties can be correlated with the microstructure, which is a result of the heat treatment: a lower second aging temperature for microstructure Ti5553-1 results in a higher strength compared to Ti5553-3. Further explanations of these results are given in section 'Effect of the size of the secondary α precipitates'.

A mechanical constitutive relationship, frequently used for titanium alloys,[12] is the Norton-Hoff model. This law was developed by Norton,[22] and was generalized to three dimensions by Hoff.[23] It defines the Von Mises equivalent stress or the yield stress $\bar{\sigma}$ in terms of the accumulated Von Mises equivalent strain $\bar{\varepsilon}$ and strain rate $\dot{\bar{\varepsilon}}$ (Eqn. (2)). The use of the Von Mises criterion is extensively justified in Ref. [2]. The material model of Eqn. (2) refers to the general three dimensions stress state, but experimental tests are uniaxial tensile tests and only the strain component along the longitudinal direction is provided. In this case the strain component is equal to the equivalent strain untill the necking event. After that, the tests are no more uniaxial and the equivalent strain cannot be determined by a single extensometer. Data after the necking event cannot be considered to identify the material model parameters if no FE inverse modelling and digital image correlation are used to identify the multiaxial stress and strain field to this paper, the stress–strain curves are stopped when the uniaxial stress reaches a maximum. According to Considére criterion, necking has not yet happened at this moment. This model takes into account many physical phenomena: strain rate dependency, hardening, softening. The law fitted on the

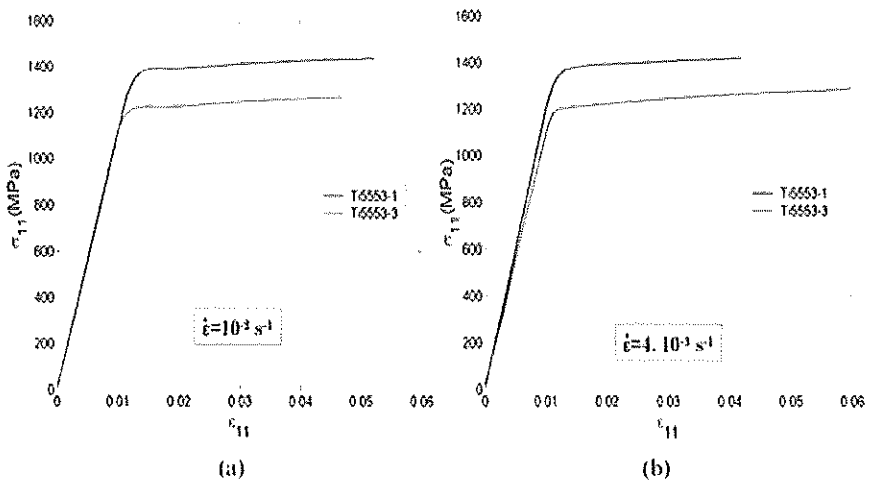

Fig. 5 Comparison between the stress–strain curves of Ti5553-1 and Ti5553-3.

basis on the uniaxial tensile tests presented in Fig. 4 is:

$$\bar{\sigma} = \exp(-P_1\bar{\varepsilon})\sqrt{3}P_2(\sqrt{3}\bar{\varepsilon})^{P_3}\dot{\bar{\varepsilon}}^{P_4}, \tag{2}$$

where:

P_1: is the softening parameter.
P_2: is a scaling factor.
P_3: is the strain rate sensitivity parameter.
P_4: is the hardening parameter.

The material parameters (P_1, P_2, P_3 and P_4) are adjusted to fit the Norton-Hoff law to the average of experimental curves. In this aim, a fitness scalar function (noted hereafter R) is defined to describe the 'distance' between the experimental results $\bar{\sigma}_S^{Exp}(\dot{\bar{\varepsilon}}, \bar{\varepsilon})$ (where s refers here to the number of the duplicate tensile tests ranging between 1 and 3) and the Norton-Hoff curve $\bar{\sigma}^{NH}(\dot{\bar{\varepsilon}}, \bar{\varepsilon})$ as evaluated with a given set of parameters values. The experimental curves and the Norton-Hoff curves are sampled at different strain positions (200 points) which are used to evaluate R as follows:

$$R(\bar{\sigma}) = \sum_{S=1}^{3}\sum_{\dot{\bar{\varepsilon}}}\sum_{\bar{\varepsilon}}\left(\bar{\sigma}_S^{Exp}(\dot{\bar{\varepsilon}}, \bar{\varepsilon}) - \bar{\sigma}^{NH}(\dot{\bar{\varepsilon}}, \bar{\varepsilon})\right)^2. \tag{3}$$

The optimal set of material parameters (P_1, P_2, P_3 and P_4) is obtained by a minimization of the fitness function R. This minimization was performed with a homemade python script involving the Nelder-Mead Simplex algorithm. For more details about this algorithm, see Ref. [24]. A better description of the script used in this algorithm is given in the Appendix.

Equation (2) contains the elastic and plastic components of the strain. However, this law does not model the beginning of the curve. The elastic part is replaced by Hooke's law:

$$\bar{\sigma}^{el} = E\bar{\varepsilon}^{el}, \tag{4}$$

where E is the Young's modulus (identified for both microstructures in section 'Elastic behaviour') and $\bar{\varepsilon}^{el}$ is the elastic strain in the tensile direction. The total model is composed of Hooke's law for elastic strain and of Norton-Hoff's law for viscoplastic strain. The later is used when the elastic linear curve intercepts that of Norton-Hoff. So for a given equivalent strain value, the corresponding equivalent stress is the minimum of the Norton-Hoff and Hooke's law as computed for that strain value.

Table 2 Norton-Hoff parameters of Ti5553-1 and Ti5553-3 microstructures

	P_1	P_2	P_3	P_4
Ti5553-1	0.00187	982	0.006	0.045
Ti5553-3	0.005	872	0.0035	0.05

These parameter values are provided in Table 2 (for the two microstructures).

It should be noted that the value of the parameter P_3 corresponding to the Ti5553-1 microstructure is larger than the value of the same parameter identified for the Ti5553-3 microstructure. This means that the Ti5553-1 microstructure is more sensitive to the strain rate than the Ti5553-3 microstructure. This can be easily observed from Fig. 4.

Table 3 summarizes the yield stress $\sigma_{p0.2}$ (experimentally measured at 0.2% of plastic strain) and the ultimate stress σ_u for each of the strain rates. The ultimate stress value is provided by an average of the stress computed from the measured sample section at rupture for each specimen (as in section 'Geometry of the specimens'). These stresses are expressed in MPa.

The results presented in Table 4 are further illustrated in Fig. 6.

Table 3 Effect of the strain rate on the experimental yield stress $\sigma_{p0.2}$

	Ti5553-1		Ti5553-3	
$\dot{\varepsilon}(s^{-1})$	$\sigma_{p0.2}$	σ_u	$\sigma_{p0.2}$	σ_u
5×10^{-5}	1285	1398	1142	1282
2×10^{-4}	1313	1419	1150	1297
4×10^{-3}	1332	1423	1185	1300
10^{-2}	1370	1452	1199	1318

Table 4 The different values of σ_{min}, σ_{max} and σ_a applied for the fatigue tests

σ_{min} (MPa)	40	66	75	86	93	110
σ_{max} (MPa)	400	660	755	866	933	1100
σ_a (MPa)	180	300	340	390	420	495

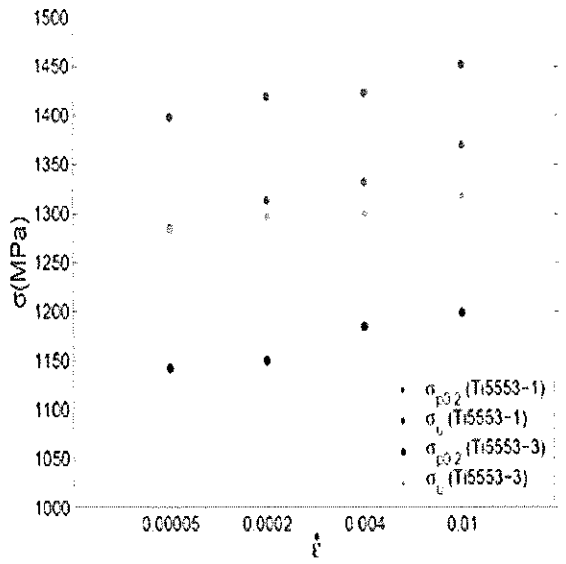

Fig. 6 Evolution of the experimental $\sigma_{p0.2}$ and the experimental σ_u as a function of $\dot{\varepsilon}$.

For information, Lutjering and Williams reported in Ref. [11] that the yield stress $\sigma_{p0.2}$ of the Ti5553 alloy is between 1090 and 1100 MPa, respectively, for a β annealed microstructure and for a bi-modal microstructure. It must be noted that the processed conditions (forging and heat treatment) used to elaborate the Ti5553 microstructures studied in Ref. [11] are not the same as the conditions used in order to elaborate the microstructures studied in the present work. This can explain the difference in the value of the yield stress between the different microstructures.

Analysis of the effect of the strain rate and the microstructure on the elastoviscoplastic behaviour

The aim of the present subsection is to analyze and interpret the effect of the strain rate and the microstructure (especially the size of the α secondary precipitates) on the mechanical behaviour (initial yield stress, ultimate stress).

Effect of the strain rate

Classically strain rate increase generates higher stress level in most materials.[25] This effect is confirmed for the two studied microstructures on the initial yield stress $\sigma_{p0.2}$ and ultimated stress σ_u. These stresses increase moderately with strain rate, which is consistent with the bibliographic results (see for example Refs [29, 30]). This strain rate effect can be explained by the theory proposed by Johnson and Gilman.[31] Johnson and Gilman relate the imposed strain rate $\dot{\varepsilon}$ to the velocity of the mobile dislocations v as:

$$\dot{\varepsilon} = \rho b v, \tag{5}$$

where ρ is the dislocation density and b is the burgers vector. The dislocation velocity is in turn related to the shear stress τ by the relation $v = (\tau/\tau_0)^{m'}$, where τ_0 and m' are material constants. Thus a higher imposed strain rate would entail a higher velocity for dislocation motion and hence a higher stress for triggering of plastic deformation at the macroscopic level.

Effect of the size of the secondary α precipitates

The effect of the size of the secondary α precipitates on the strength (initial yield stress $\sigma_{p0.2}$ and the ultimated stress σ_u) can be explained by the Hall-Petch effect.[25,26] This relation assumes that the yield stress is inversely proportional to the square root of the grain size. Physically this effect assumes that the grain boundaries between the β phase and the secondary α precipitates act as barriers to dislocation motion. As the size of secondary α precipitates is smaller and their number is higher in the microstructure Ti5553-1 than in the Ti5553-3 microstructure, there are more a barriers in the first microstructure than in the second one. So the stress required to move the dislocations is higher for Ti5553-1 microstructure.

DAMAGE PROPERTIES OF THE Ti5553 MICROSTRUCTURES

Geometry of the specimens

It is common to study the damage of materials on the basis of experimental tensile tests on notched axisymmetric specimens. In this study, tests were performed on

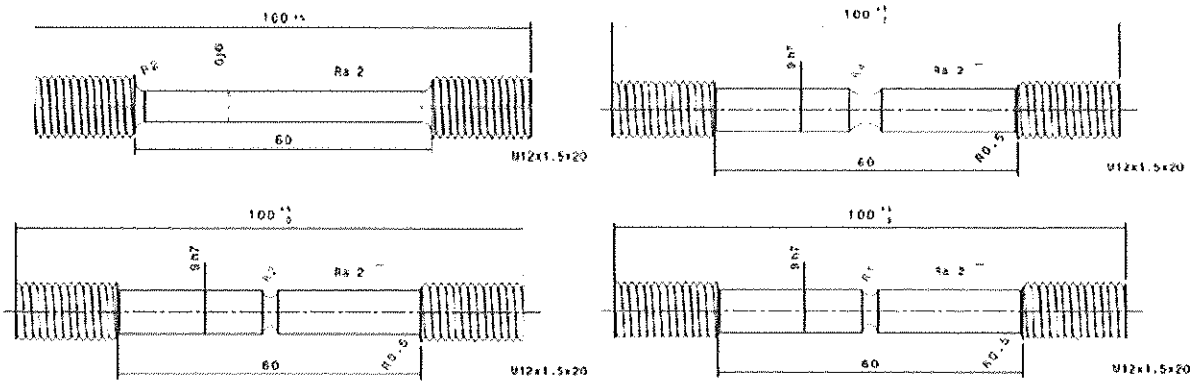

Fig. 7 Geometry of the smooth and notched tensile specimens.

samples with three different notch root initial radii R_0 equal to 1, 2 and 4 mm. The initial diameter in the gauge section was kept constant at 6 mm for all specimens tested. The geometry of the notched specimens is provided in Fig. 7. The different notches induce different levels of hydrostatic tension (which induce different triaxiality levels) in the specimens during straining, which distinctly affect both the true stress and the strain to failure of the material. Three duplicate tests were conducted for each case (each temperature, notch radius, alloy and microstructure). During the tests, the applied load, the crosshead displacement and the diameter reduction (at the minimum cross-section) were continuously measured.

The ductility of the material, defined by the true fracture strain ε_f is computed by the following relation:

$$\varepsilon_f = Ln(A_0/A_f), \tag{6}$$

where A_0 and A_f are the initial and final sections of the specimen. The initial section A_0 was exactly measured prior to testing.

Experimentally, the minimum cross-section after fracture A_f is determined by using optical microscopic measurement available in MMS laboratory of ULg.

Experimental results

Effect of the notch radius on the axial stress–strain curve

The effect of the notch radius on the experimental axial stress component versus the tensile strain, for smooth and notched round specimens is given in Fig. 8 (three curves for each radius corresponding to the three duplicated tests). The stress is calculated by dividing the experimental force by the area of the current minimum notch cross-section. The curves are interrupted at the maximum stress. The main trend that the stress increases with decreasing initial notch radius is also well captured in FE simulations. Note that the apparent elastic modulus (the slope of the stress–strain curve) increases also with triaxiality.

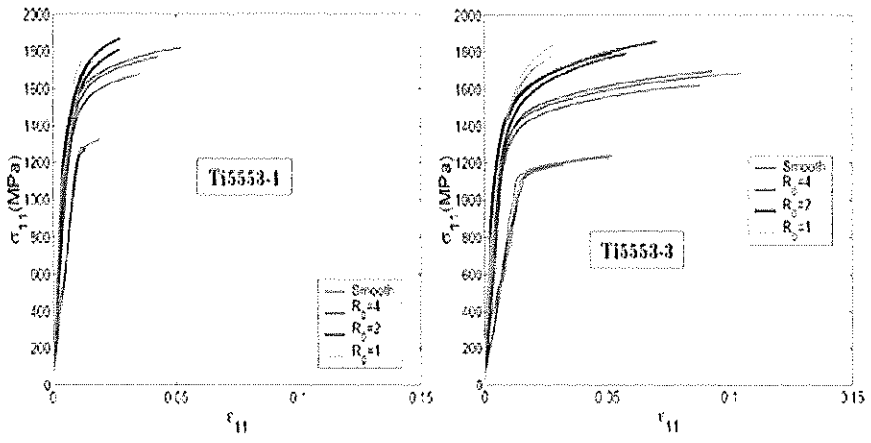

Fig. 8 Effect of the initial notch radius on the stress–strain curves.

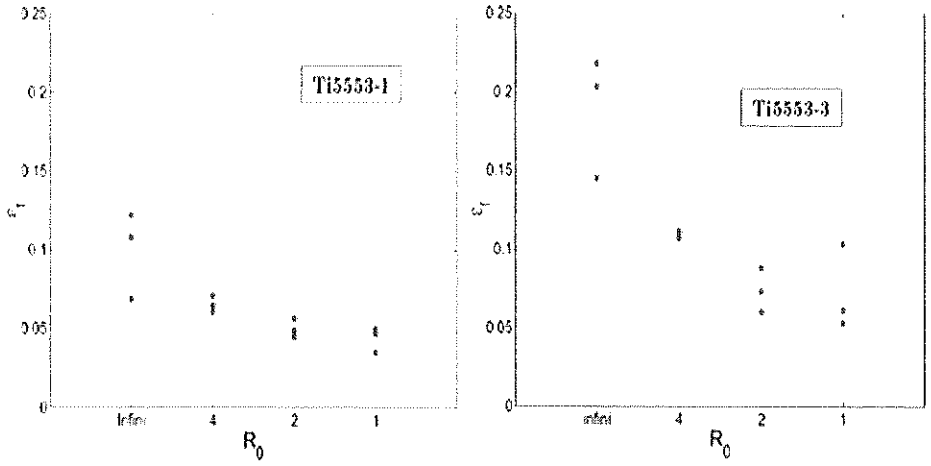

Fig. 9 Effect of the initial notch radius on the fracture strain.

Effect of the initial notch radius on the fracture strain

The fracture strain, experimentally determined according to Eqn. (6), is plotted as a function of the initial notch radius (over the minimum necking section). As expected, it is apparent from the results of Fig. 9 that the ductility of the tested microstructures is strongly dependent on the value of the initial notch radius. The triaxiality in the minimum section is inversely proportional to the notch radius. It is demonstrated in many scientific works and theories[27,28] that ductility at failure and triaxiality are nonlinearly inversely proportional: the more stress state is triaxial, the less the strain at failure is. So the fracture strain is nonlinearly proportional to the notch radius. This result is experimentally observed. Indeed, it is seen that the specimen with 4 mm initial notch radius has globally larger strain to fracture than the specimens with initial notch radius equal to 1 and 2 mm, respectively. The expected general tendency for fracture strain to increase with increasing notch profile radius is clear but there is a lot of scattering in the results. This large dispersion in fracture strain is also observed for other titanium alloys, like the Ti-6Al-4V alloy (see Ref. [3]). This dispersion may be due to a non-controlled difference in the microstructure elaboration or heat treatment (inducing for example a non-controlled heterogeneity of the grain size...). Unfortunately, we are not able at this level to give a definitive confirmation to the explanation of this phenomenon. Further investigation is required in order to better understand this dispersion.

The grain boundary of the secondary α precipitates is detrimental to tensile ductility of the Ti5553 alloy. Indeed high stress concentration and local strain occur at this grain boundary, especially at triple points. In these regions, crack initiates and propagates along grain boundaries and fracture occurs even at low macroscopic strains. As the numerical density of the secondary alpha precipitates is statistically higher (in the case of the Ti5553-1 microstructure compared to the Ti5553-3 microstructure, the fracture occur earlier in the first microstructure.

FATIGUE EXPERIMENTS AND RESULTS

Geometry of the specimens

The geometry of the fatigue specimens is presented in Fig. 10. Cylindric specimens were extracted from the pancakes (one pancake from each microstructure) by the MSM laboratory at ULg, using the electric discharge machining technique (Fig. 11). The specimens were finally

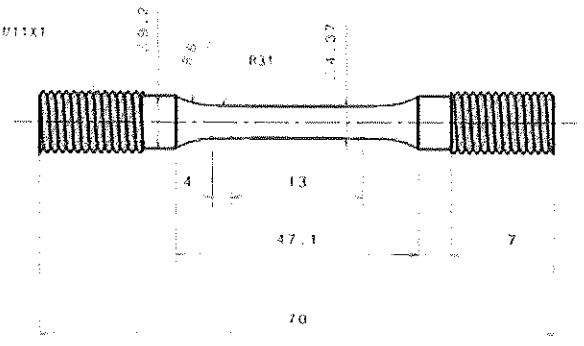

Fig. 10 Geometry of the Ti5553 fatigue specimens.

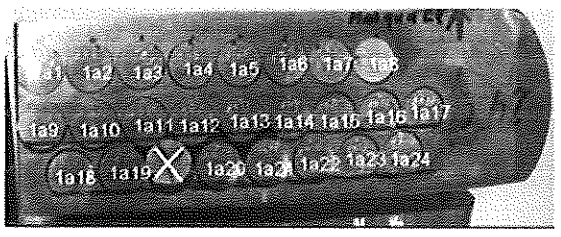

Fig. 11 Extraction of the specimens from the initial pancakes.

machined by the Metcut Research Inc (Cincinnati, Ohio, USA) to meet the machining standards of Techspace Aero. Forty-nine specimens were machined: 24 specimens of the Ti5553-1 microstructure and 25 specimens of Ti5553-3. Forty specimens were tested at the ULg laboratory (20 specimens for each microstructure) and 9 at Metcut Research Inc (a laboratory qualified to carry out fatigue tests) in order to compare the results between them.

HCF tests

High-cycle fatigue (HCF) tests were conducted, in accordance with the ASTM E466–02 standard, at room temperature and with a stress ratio R ($\sigma_{min}/\sigma_{max}$) of 0.1, where σ_{min} and σ_{max} are, respectively, the minimum and the maximum stress during the loading cycle. The different values of σ_{min}, σ_{max} and the magnitude stress $\sigma_a = (\sigma_{max} - \sigma_{min})/2$ are given in Table 4. A sinusoidal loading was applied at a frequency of 125 and 80 Hz at ULg and Metcut, respectively. The analyzed domain ranged from 10^4 to 2×10^7 cycles. If a sample reached 2×10^7 cycles without failure, the test was stopped and the sample was considered unbroken ('run out' on the Wöhler curves).

EXPERIMENTAL RESULTS OF THE FATIGUE TESTS OF THE Ti5553 MICROSTRUCTURES

Wöhler curves

High-cyclic fatigue tests are the most widely used technique to establish the fatigue limit of a chosen metal by essentially generating the S-N, or the Wöhler, curve [the evolution of the alternated stress σ_a with the number of cycles to failure (NR)]. The identified S-N curves of the two investigated microstructures are presented in Fig. 12. Only the results corresponding to the ULg tests are presented here. Curves were built by the Techspace Aero company using a simple Bastenaire model.[32] For each stress level, a minimum of three specimens were tested.

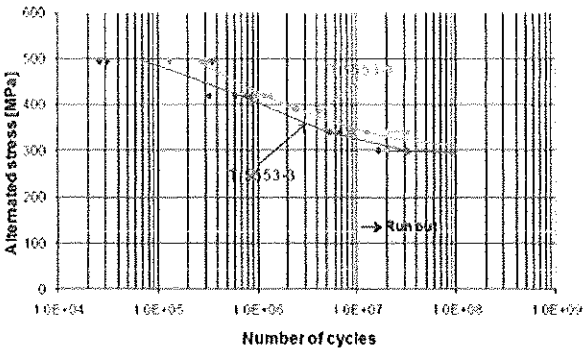

Fig. 12 S-N curves (Wöhler) of the Ti5553 microstructures.

Table 5 Correlation between the static properties and the fatigue properties of the Ti5553 alloy

	Ti5553-1	Ti5553-3
$\sigma_{p0.2}$ at $\dot{\varepsilon} = 4 \times 10^{-3}$ s^{-1}	1332	1185
σ_u at $\dot{\varepsilon} = 4 \times 10^{-3}$ s^{-1}	1423	1300
Fatigue limit at $2.* 10^7$	330	310
Fatigue limit/$\sigma_{p0.2}$	0.261	0.275
Fatigue limit/σ_u	0.244	0.251

As indicated in Fig. 12, Ti5553-1 exhibits a slightly higher endurance limit than Ti5553-3. It should be noted that the experimental results obtained at ULg were similar to the results obtained at Metcut Research Inc. The 'run out' of the Ti5553-1 and the Ti5553-3 occurred at 340 and 300 MPa, respectively. The endurance limit defined at 2×10^7 was equal to 348 and 326 MPa for the Ti5553-1 and Ti5553-3 microstructures, respectively.

The comparison of the fatigue properties of the two microstructures may be correlated with a similar trend noticed for the tensile strength of the two microstructures in Table 5. From this table, it is clear that an increase in tensile strength led to an increase in fatigue strength. It is interesting to note that a decrease in the size of the secondary α precipitates have a positive effect on the yield and tensile strength (Hall-Petch effect as mentioned in section 'Effect of the size of the secondary α precipitates') while generally improving fatigue strength by retarding the crack initiation. The enhanced resistance to crack initiation is considered as a result of high strength of fine grains that act as potential obstacles for dislocation movement, and thereby the formation of microcracks is inactive.[16,33–37]

In conclusion, the fatigue behaviour of the two microstructures of the Ti5553 alloy is linked to changes in the microstructures that occur as a result of small modifications in heat treatment. After analysis, it seems that no clear relationship between the fatigue limit and the initial position of the extracted specimen in the pancake can be observed.

Fractographic analysis

The fatigue fracture surfaces were observed with a scanning electron microscope in order to understand the fracture mode. From this examination (see Fig. 13), it is clear that the majority of the specimens (from the two microstructures) present a crack initiation on α nodules depleted in chromium and molybdenum. From the same examination, fatigue crack initiation generally seems to occur at grain boundaries or at a triple point. No significant clear difference is found between the fracture mechanisms of the two microstructures. These conclusions are

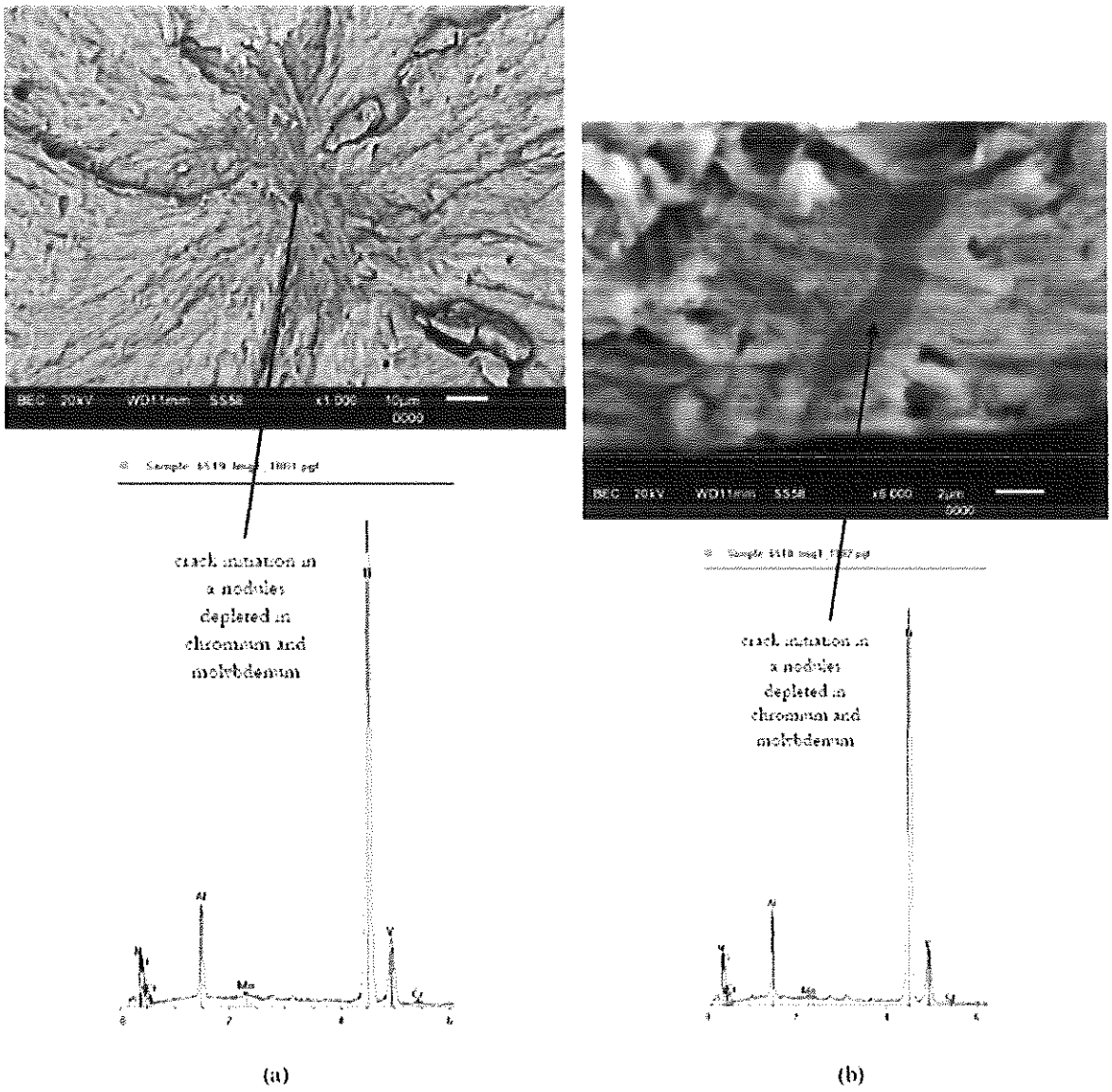

Fig. 13 Fracture surfaces of Ti5553-1 specimens.

drawn from analysis of 10 specimens from the Ti5553-1 microstructure and 8 specimens from the Ti5553-3 microstructure.

COMPARISON OF FATIGUE RESULTS OF THE TWO STUDIED Ti5553 ALLOY MICROSTRUCTURES WITH THOSE OF TWO OTHER TITANIUM ALLOYS, Ti40 AND Ti-6Al-4V

Fatigue properties of Ti40 and Ti-6Al-4V

- Ti40 is a commercially pure low-iron grade 2 titanium containing 0.03% iron or less.[38] The alloy is double vacuum melted by the consumable electrode arc melting process. Russo and Schöbel[39] studied Ti40 ingots forged and rolled into a 44.4 or 50.8 mm thick plate product. The plate product was annealed at 730 °C for 30 min and air cooled. The frequency of the fatigue tests corresponding to the Ti40 was set to 20 Hz. The stress ratio R was equal to 0.1 and the fatigue tests were performed at room temperature. The yield stress (resp. the ultimate stress) of this alloy in the heat treatment conditions cited previously is about 960 MPa (resp. 985 MPa) as mentioned in Ref. [40].
- Bellows et al.[41] studied Ti-6Al-4V, an alloy forged into fan blade forging tools, measuring approximately 400 × 150 × 20 mm, in a single forging campaign by the Cleveland Operations of Textron Turbine Engine Components. The forging stock had been double vacuum arc remelted, converted to 64 mm diameter bar stock, and supplied in the

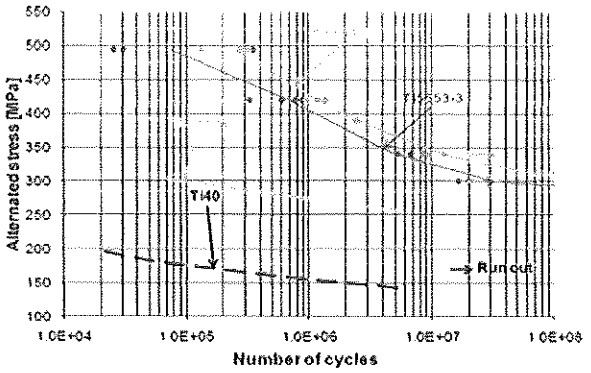

Fig. 14 S-N curves of Ti5553, TA6V and Ti40 alloys ($R = 0.1$).

mill-annealed condition in accordance with AMS4928L.[42] The frequency of the fatigue tests corresponding to the Ti-6Al-4V was set to 60 Hz. The stress ratio R was equal to 0.1 and the fatigue tests were performed at room temperature. The yield stress (resp. the ultimate stress) of this alloy is about 1100 MPa (resp. 1170 MPa).

It is clear that the yield stress and the ultimate stress of the titanium alloys depend on their chemical composition, heat treatment and the applied strain rate. But it can be concluded, despite the dispersion, that the strength (yield stress and ultimate stress) of the Ti5553 alloy (both microstructures) is superior to the strength of the Ti-6Al-4V alloy which is superior to the strength of the Ti40 alloy.

S-N curves

A comparison of the fatigue test results obtained in this research study with the S-N curves of the above alloys Ti40 and Ti-6Al-4V is shown in Fig. 14. It demonstrates that the high-cycle fatigue resistance of both Ti5553 microstructures is noticeably better than the high-cycle fatigue resistance of the Ti40 and Ti-6Al-4V alloys. This result can be explained by the difference of the yield stress and the ultimate stress between the different alloys. Indeed an increase in the yield stress and the ultimate stress is accompanied by an increase in the fatigue strength.

The fatigue strength of Ti5553 (fatigue limit equal to 429 MPa at 10^6 cycles and 404 MPa at 10^6 cycles for the Ti5553-1 and Ti5553-3 microstructures, respectively) is largely superior to the limit fatigue (at 10^6 cycles) of the Ti40 alloy (equal to 155 MPa) and of the Ti-6Al-4V (equal to 274 MPa).

Goodman diagrams

Several models are traditionally been used for constant life diagrams; the first and probably the most popular is

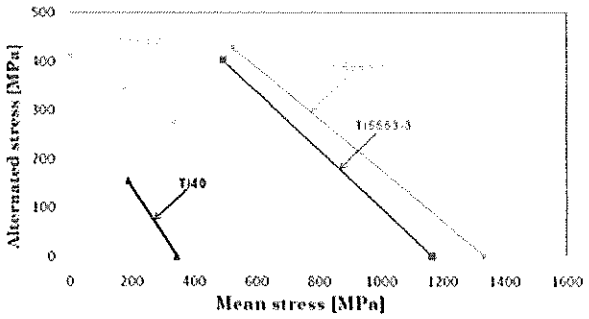

Fig. 15 Goodman diagrams of Ti5553, TA6V and Ti40 alloys.

the Goodman diagram.[43,44] In this case, the magnitude stress σ_a is plotted as a function of the mean stress σ_m in the following way:

$$\sigma_a = \sigma_a(\sigma_m = 0) * \left(1 - \frac{\sigma_m}{\sigma_u}\right), \tag{7}$$

where $\sigma_a = \sigma_a(\sigma_m = 0)$ is the limit fatigue for completely reversed loading and σ_u is the ultimate tensile stress.

In Fig. 15, the Goodman diagram corresponding to the different alloys and microstructures studied in Fig. 14 is constructed at 10^6 cycles and at room temperature with available data. So, in the case of Ti5553-1, Ti5553-3 and Ti40, a straight line is drawn connecting the point (σ_m, σ_a) determined from Fig. 14 at 10^6 cycles to the ultimate tensile strength on the mean axis. In the case of Ti-6Al-4V, a straight line is drawn connecting the point (σ_m, σ_a) determined at 10^6 cycles from Fig. 14 (so at $R = 0.1$) with the point (σ_m, σ_a) determined at 10^6 cycles from Ref. [41] at a stress ratio of $R = -1$ (the Ti-6Al-4V specimens used for the two stress ratios 0.1 and -1 came from the same supplier).

Figure 15 undoubtedly confirms the superiority of the fatigue properties of the Ti5553 alloys in comparison with the other alloys.

CONCLUSIONS

This paper presents and discusses the experimental results of a recent experimental study aimed to determine the static (elastoviscoplastic and damage) and high-cycle fatigue behaviour of two distinguish microstructures of the new Ti5553 titanium alloy. The difference between the two microstructures is related to the value of the temperature of the second aging which induces a difference of the size of the secondary α phase. It is interesting to note that a decrease in the size of the secondary α precipitates have a positive effect on the yield and tensile strength (Hall-Petch effect as mentioned in section 'Effect of the size of the secondary α precipitates') and a negative effect of the ductility while generally improving fatigue

strength by delaying the crack initiation. The enhanced resistance to crack initiation is considered as a result of high strength of fine grains that act as potential obstacles for dislocation movement, and thereby the formation of microcracks is less inactive. A fractographic analysis is carried out in order to understand the fatigue mechanisms in both microstructures (Ti5553-1 and Ti5553-3). This analysis reveals that fatigue crack initiation generally seems to occur at grain boundaries or at a triple points and no significant clear difference was found between the fracture mechanisms of the two microstructures. The static and fatigue properties of Ti5553 were also compared with the fatigue properties of two other titanium alloys, Ti40 and Ti-6Al-4V. The results of various studies have shown that the Ti5553 alloy exhibits substantially superior static and fatigue characteristics relative to other titanium alloys and in particular in comparison with the Ti-6Al-4V alloy, which is the most popular titanium alloy. This comparison confirms the well-known idea stating that an increase of the yield stress and the ultimate stress is accompanied by an increase in the fatigue strength. This makes Ti5553 a promising material for advanced aeronautical applications.

Acknowledgements

The authors thank the Walloon Region (Winnomet Titaero Project), the Belgian Scientific Research Fund FNRS, which finances A.M.H., and the Interuniversity Attraction Poles Program, Belgian Science Policy P7, for their financial support.

REFERENCES

1 Srivatsan, T. S., Soboyejo, W. O. and Lederich, R. J. (1995) The cyclic fatigue and fracture behavior of a titanium alloy metal matrix composite. *Eng. Fract. Mech.* **52**, 467–491.
2 Ben Bettaieb, M., Van Hoof, T., Dufour, P., Lenain, A., Jacques, P.-J. and Habraken, A.-M. Comparison between the mechanical behavior of Ti6Al4V and Ti5553 alloys. Part I: elasticity, viscoplasticity and plastic anisotropy. *Mater. Sci. Eng. A* (submitted).
3 Ben Bettaieb, M., Van Hoof, T., Minnebo, H., Dufour, P., Lenain, A. and Habraken, A.-M. Comparison between the mechanical behavior of Ti6Al4V and Ti5553 alloys. Part II: damage characterization and numerical validations. *Mater. Sci. Eng. A* (submitted).
4 Clement, N. (2010) Phase transformations and mechanical properties of the Ti-5553 b-metastable titanium alloy, PhD Thesis, UCL, Belgium.
5 Li, S. J., Cui, T. C., Hao, Y. L. and Yang, R. (2008) Fatigue properties of a metastable beta-type titanium alloy with reversible phase transformation. *Acta Biomater.* **4**, 305–317.
6 Lin, C.-W., Ju, C.-P. and Chern Lin, J.-H. (2005) A comparison of the fatigue behavior of cast Ti–7.5Mo with c.p. titanium, Ti–6Al–4V and Ti–13Nb–13Zr alloys. *Biomaterials* **26**, 2899–2907.
7 Gerday, A. F. (2009) Mechanical behavior of Ti-5553 alloy: modeling of representative cells, PhD Thesis, ULg, Belgium.
8 Boyer, R. R. and Briggs, R. D. (2005) The use of β titanium alloys in the aerospace industry. *J. Mater. Eng. Perform.* **14**, 681–685.
9 Arrazola, P. J., Garay, A., Iriarte, L.-M., Armendia, M., Marya, S. and Le Maître, F. (2009) Machinability of titanium alloys (Ti6Al4V and Ti555.3). *J. Mater. Process. Technol.* **209**, 2223–2230.
10 Casavola, C., Pappalettere, C. and Tattoli, F. (2009) Experimental and numerical study of static and fatigue properties of titanium alloy welded joints. *Mech. Mater.* **41**, 231–243.
11 Lütjering, G. and Williams, J. C. (2007) *Titanium*. 3nd edn. Springer-Verlag, Berlin.
12 Sarrazin-Baudoux, C. (2005) Abnormal near-threshold fatigue crack propagation of Ti alloys: role of the microstructure. *Int. J. Fatigue* **27**, 773–782.
13 Berteaux, O., Jouiad, M., Thomas, M. and Hénaff, G. (2006) Microstructure-low cycle fatigue behaviour relationships in a PM γ-TiAl alloy. *Intermetallics* **14**, 1130–1135.
14 Kumpfert, J., Kimb, Y. W. and Dimiduk, D. M. (1995) Effect of microstructure on fatigue and tensile properties of the gamma TiAl alloy Ti-46.5A1–3.ONb-2.1Cr-0.2W. *Mater. Sci. Eng. A* **192/193**, 465–473.
15 Marmy, P., Leguey, T., Belianov, I. and Victoria, M. (2000) Tensile and fatigue properties of two titanium alloys as candidate materials for fusion reactors. *J. Nucl. Mater.* **283–287**, 602–606.
16 Nakajima, K., Terao, K. and Miyata, T. (1998) The effect of microstructure on fatigue crack propagation of $\alpha+\beta$ titanium alloys in-situ observation of short fatigue crack growth. *Mater. Sci. Eng. A* **243**, 176–181.
17 Srivatsana, T. S., Bathinib, U., Patnaikb, A. and Quick, T. (2010) A study of cyclic fatigue, damage initiation, damage propagation, and fracture of welded titanium alloy plate. *Mater. Sci. Eng. A* **527**, 6649–6659.
18 Fujita, T., Ishikawa, M., Hashimoto, S., Minakawa, K. and Ouchi, C. (1993) Beta Titanium Alloys in the 1990's. In: *Proceedings of the Symposium, TMS Annual Meeting*, Denver, CO, USA, pp. 297–307.
19 Polmear, I. J. (1995) *Light Alloys*, Arnold, London.
20 Kubiak, K. and Sieniawski, J. (1998) Development of the microstructure and fatigue strength of two phase titanium alloys in the processes of forging and heat treatment. *J. Mater. Process. Technol.* **78**, 117–121.
21 Millet, Y. (2007) Famille des alliages de titane. Bonnes pratiques & interdits, *Journées Technologiques TITANE*, Nantes, France.
22 Norton, F. H. (1929) *Creep of Steel at High Temperature*. Mc Grow-Hill, New-York.
23 Hoff, N. J. (1954) Approximate analysis of structure in the presence of moderately large creep deformation. *Q. Appl. Math.* **12**, 49–55.
24 Nelder, J. and Mead, R. (1965) A simplex method for function minimization. *Comput. J.* **7**, 308–313.
25 Hall, E. O. (1951) The deformation and ageing of mild steel: III discussion of results. *Proc. Phys. Soc. Sec. B.*, **64**, 747–753.
26 Petch, N. J. (1953) The cleavage strength of polycrystals. *J. Iron Steel Inst.* **174**, 25–28.

27 Rice, J. R. and Tracey, D. M. (1969) On the ductile enlargement of voids in triaxial stress fields. *J. Mech. Phys. Solids.* **17**, 201–217.
28 Hancock, J. W. and Meckenzie, A. C. (1976) On the mechanisms of ductile failure in high strength steels subjected to multi-axial stress-states. *J. Mech. Phys. Solids.* **24**, 147–169.
29 Semiatin, S. L. and Bieler, T. R. (2001) The effect of alpha platelet thickness on plastic flow during hot working of Ti-6Al-4V with a transformed microstructure. *Acta Mater.* **49**, 3565–3573.
30 Venkatesh, B. D., Chen, D. L. and Bhole, S. D. (2009) Effect of heat treatment on mechanical properties of Ti-6Al-4V ELI alloy. *Mat Sci Eng A-Struct* **506**, 117–124.
31 Johnston, W. G. and Gilman, J. J. (1959) Dislocation velocities, dislocation densities, and plastic flow in lithium fluoride crystals. *J. Appl. Phys.* **30**, 129–144.
32 Bastenaire, F. A. (1972) New method for the statistical evaluation of constant stress amplitude fatigue-test results. Probabilistic aspects of fatigue. *ASTM STP* **511**, 3–28.
33 Tokaji, K., Ogawa, T. and Ohya, K. (1992) The effect of grain size on small fatigue crack growth in pure titanium. *Trans. JSME* **58**, 178–185.
34 Turner, N. G. and Roberts, W. T. (1968) Fatigue behavior of titanium. *AIME Trans.* **242**, 1223–1230.
35 Lucas, J. J. and Konieczny, P. P. (1971) Relationship between alpha grain size and crack initiation fatigue strength in Ti-6Al-4V. *Metall. Mater. Trans. B.* **2**, 911–912.
36 Stubbington, C. A. and Bowen, A. W. (1973) The effect of section size on the fatigue properties of Ti-6 Al-4 V bars. In: *Proceedings of the Second International Conference*. Cambridge, Mass, USA, pp. 1283–1296.
37 Wagner, L. and Lutjering, G. (1987) Microstructural influence on propagation behavior of short cracks in an (alpha+ beta) titanium alloy. *Z. Metallkd.* **78**, 369–375.
38 Boyer, R., Collings, E. W. and Welsch, G. (1994) Materials Properties Handbook: Titanium Alloys. ASM International, Ohio, USA.
39 Russo, P. A. and Schöbel, J. D. (1982) Mechanical properties of commercially pure titanium containing low iron, presentation at ACHEMA82, Franckfurt, West Germany.
40 Xin, S. W., Zhao, Y. Q. and Zeng, W. D. (2007) Effect of heat treatment on thermal stability of Ti40 alloy. *Trans. Nonferrous Met. Soc. China* **17**, 526–531.
41 Bellows, R. S., Muju, S. and Nicholas, T. (1992) Validation of the step test method for generating Haigh diagrams for Ti–6Al–4V. *Int. J. Fatigue* **21**, 687–697.
42 Aerospace materials specification 'titanium alloy bars, wire, forgings and rings, 6Al-4V, annealed'. Warrendale (PA): SAE International, Society of Automotive Engineers. 1990.
43 Goodman, J. (1991) Mechanics Applied to Engineering. Longmans Green, London, 1899 (as referenced in S. Suresh (1991) Fatigue of Materials. Cambridge University Press, Cambridge).
44 Sendeckyj, G. P. (1998) History of constant life diagrams. In: *High Cycle Fatigue of Structural Materials* (Edited by T. S. Srivatsan and W. O. Soboyejo), TMS, Warrendale, PA, USA, pp. 95–107.

APPENDIX: DETAILED DESCRIPTION OF THE NELDER–MEAD ALGORITHM

Nelder-Mead method

A simplex method for finding a local minimum of a function of several variables has been designed by Nelder and Mead.

For two variables, a simplex is a triangle, and the method is a pattern search that compares function values at the three vertices of a triangle. The worst vertex, where $f(x, y)$ is largest, is rejected and replaced with a new vertex. A new triangle is formed and the search is continued. The process generates a sequence of triangles (which might have different shapes), for which the function values at the vertices get smaller and smaller. The size of the triangles is reduced and the coordinates of the minimum point are found.

The Nelder and Mead's algorithm is stated using the term *simplex* (a generalized triangle in N dimensions) and will find the minimum of a function of N variables. It is effective and computationally compact.

Initial triangle BGW

Let $f(x, y)$ be the function that is to be minimized. To start, we are given three vertices of a triangle: $Vk = (xk, yk)$, $k = 1, 2, 3$. The function $f(x, y)$ is then evaluated at each of the three points: $zk = f(xk, yk)$ for $k = 1, 2, 3$. The subscripts are then reordered so that $z1 \leq z2 \leq z3$. We use the notation

$$B = (x1, y1), \quad G = (x2, y2), \quad \text{and} \quad W = (x3, y3) \tag{A.1}$$

to help remember that B is the best vertex, G is good (next to best), and W is the worst vertex.

Midpoint of the good side

The construction process uses the midpoint of the line segment joining B and G. It is found by averaging the coordinates:

$$M = \frac{B + G}{2} = \left(\frac{x_1 + x_2}{2}, \frac{y_1 + y_2}{2} \right). \tag{A.2}$$

Reflection using the point R

The function decreases as we move along the side of the triangle from W to B, and it decreases as we move along the side from W to G. Hence it is feasible that $f(x, y)$ takes on smaller values at points that lie away from W on the opposite side of the line between B and G. We choose a test point R that is obtained by 'reflecting' the triangle through the side BG. To determine R, we first find the

midpoint M of the side BG. Then draw the line segment from W to M and call its length d. This last segment is extended a distance d through M to locate the point R. The vector formula for R is

$$R = M + (M - W) = 2M - W. \tag{A.3}$$

Expansion using the point E

If the function value at R is smaller than the function value at W, then we have moved in the correct direction towards the minimum. Perhaps the minimum is just a bit farther than the point R. So we extend the line segment through M and R to the point E. This forms an expanded triangle BGE. The point E is found by moving an additional distance d along the line joining M and R. If the function value at E is less than the function value at R, then we have found a better vertex than R. The vector formula for E is:

$$E = R + (R - M) = 2R - M. \tag{A.4}$$

Contraction using the point C

If the function values at R and W are the same, another point must be tested. Perhaps the function is smaller at M, but we cannot replace W with M because we must have a triangle. Consider the two midpoints $C1$ and $C2$ of the line segments WM and MR, respectively. The point with the smaller function value is called C, and the new triangle is BGC.

Note: The choice between $C1$ and $C2$ might seem inappropriate for the two-dimensional case, but it is important in higher dimensions.

Shrink towards B

If the function value at C is not less than the value at W, the points G and W must be shrunk towards B. The point G is replaced with M, and W is replaced with S, which is the midpoint of the line segment joining B with W.

Logical decisions for each step

A computationally efficient algorithm should perform function evaluations only if needed. In each step, a new vertex is found, which replaces W. As soon as it is found, further investigation is not needed, and the iteration step is completed. The logical details for two-dimensional cases are explained in the following table.

IF $f(R)<f(G)$, THEN Perform Case (i) {either reflect or extend}
ELSE Perform Case (ii) {either contract or shrink}

BEGIN {Case (i).}	BEGIN {Case (ii).}
IF $f(B)<f(R)$ THEN	IF $f(R)<f(W)$ THEN
replace W with R	replace W with R
ELSE	Compute $C=(W+M)/2$
	or $C=(W+M)/2$ and $f(C)$
Compute E and f(E)	IF $f(C)<f(W)$ THEN
IF $f(E)<f(B)$ THEN	replace W with C
replace W with E	ELSE
ELSE	Compute S and $f(S)$
replace W with R	replace W with S
ENDIF	replace G with M
ENDIF	ENDIF
END {Case (i).}	END {Case (ii).}